Materials Advances

ROYAL SOCIETY OF CHEMISTRY

PAPER

View Article Online
View Journal | View Issue

Cite this: *Mater. Adv.*, 2022, 3, 4243

Diverse catalytic behavior of a dye-based polymer metal-free catalyst for hydrogen peroxide photoproduction†

Qiang Hong,‡[a] Qingyao Wu,‡[b] Zhenyu Wu,[a] Yan Liu,[a] Yi Li,[a] Hui Huang, *[a] Yang Liu*[a] and Zhenhui Kang *[ac]

Metal-free polymer-based catalysts have shown promising photocatalytic performance for efficient hydrogen peroxide (H_2O_2) photoproduction under visible light. However, the structure of the active site and the interface charge transfer of these catalysts have not been revealed clearly. Here, we report the fabrication of four narrow bandgap single-dye-based polymer metal-free catalysts (PPC-*X*, *X* = 75, 100, 125, 175). The catalyst PPC-*X* was synthesized by a hydrothermal method using proanthocyanidin (OPC) as the raw material. The reaction temperature was set at 75 °C, 100 °C, 125 °C, and 175 °C, and finally, the single-dye polymer catalyst was obtained, which was marked as PPC-*X*, with *X* representing the polymerization temperature. The PPC-*X* as catalysts show diverse catalytic behavior for H_2O_2 photoproduction. Under visible light excitation, the PPC-*X* catalysts (*X* = 100, 125, 175) reduced O_2 to produce H_2O_2 *via* the two-electron transfer pathway and oxidized water to release O_2 by the four-electron transfer pathway. For the PPC-75 catalyst, O_2 was reduced by photo-generated electrons on the catalyst surface *via* the two-electron transfer pathway, while the PPC-75 catalyst itself also serves as a sacrificial agent to consume the photo-generated holes, leading to a high H_2O_2 production. The H_2O_2 yield of PPC-75 is 1152 μmol g^{-1} h^{-1}, and that of PPC-100 is up to 1214 μmol g^{-1} h^{-1} at a light intensity of 32.6 mW cm^{-2}. This work provides a practical research example and idea for the in-depth understanding and design of efficient polymer-based photocatalysts.

Received 13th February 2022,
Accepted 2nd April 2022

DOI: 10.1039/d2ma00162d

rsc.li/materials-advances

1. Introduction

Hydrogen peroxide (H_2O_2), as a clean high-energy oxidant, has been widely used in medicine, chemistry, and environmental management.[1–5] Moreover, it has attracted more and more attention in the past decade because of its potential to replace fossil fuels.[6–10] The synthesis of H_2O_2 through photocatalysis and direct conversion of solar energy into chemical energy is a cost-effective, safe and green production route.[11–14] Previous studies have shown that metal–semiconductor catalysts have achieved remarkable progress in the photosynthesis of H_2O_2.[15–19] Typically, the catalysts for the photoproduction of H_2O_2 can be divided into metal catalysts and metal-free catalysts. Metal-free catalysts are regarded as promising catalysts due to their low cost, environmental friendliness, and sustainability.[20–25] Metal-free catalysts are mainly carbon-based materials such as g-C_3N_4, GO, CDs, COFs, and metal-free polymer catalysts.[26–31] At present, the generation of H_2O_2 with metal-free photocatalysts represented by modified g-C_3N_4 is much higher among all kinds of semiconductor materials; for example, the H_2O_2 production rate of the catalyst obtained through the hybridization of g-C_3N_4 with CNTs is 32.6 μmol h^{-1}.[31–34] In addition to g-C_3N_4, there are several kinds of metal-free polymer catalysts with excellent photocatalytic performance.[35,36] Shiraishi *et al.* reported a metal-free catalyst, resorcinol formaldehyde resins, for efficient H_2O_2 photoproduction, which has a strong absorption at 700 nm with a solar to chemical energy conversion rate (SCC) up to 0.5%.[37] Liang *et al.* introduced acetylene or diacetylene moieties into covalent triazine frameworks, which promoted the charge separation in the conjugated structures, subsequently improving the catalytic efficiency.[38] Moreover, in the polymer-based metal-free catalyst system, numerous issues, such as the active site structure,

[a] *Institute of Functional Nano & Soft Materials (FUNSOM), Jiangsu Key Laboratory for Carbon-Based Functional Materials & Devices, Soochow University, 199 Ren'ai Road, Suzhou, 215123, China. E-mail: hhuang0618@suda.edu.cn, yangl@suda.edu.cn*
[b] *Key Laboratory of Chemical Biology of Hebei Province, College of Chemistry and Environmental Science, Hebei University, Baoding 071002, China*
[c] *Macao Institute of Materials Science and Engineering (MIMSE), MUST-SUDA Joint Research Center for Advanced Functional Materials, Macau University of Science and Technology, Taipa 999078, Macao, China. E-mail: zhkang@suda.edu.cn*

† Electronic supplementary information (ESI) available. See DOI: https://doi.org/10.1039/d2ma00162d

‡ These authors contributed equally.

reaction mechanism, and catalyst interface charge transfer, have not been revealed clearly.

In this study, we selected the organic dye molecule (proanthocyanidin, OPC) as the raw material and fabricated the narrow bandgap single-dye-based polymer metal-free catalysts (PPC-*X*; *X* denotes the reaction temperature) by a hydrothermal self-polymerization method. In the present system, the H_2O_2 yield of PPC-75 is 1152 μmol g^{-1} h^{-1}, and that of the best sample PPC-100 is 1214 μmol g^{-1} h^{-1} at a light intensity of 32.6 mW cm^{-2}. We used cyclic voltammetry (CV) and transient photovoltage (TPV) tests to reveal the diverse catalytic behavior of dye-based polymer metal-free catalysts for H_2O_2 photoproduction. Under visible light excitation, the catalyst PPC-*X* (*X* = 100, 125, 175) reduced O_2 to produce H_2O_2 *via* the two-electron transfer pathway and oxidized water to release O_2 by the four-electron transfer pathway. For the PPC-75 catalyst, the O_2 was reduced by photo-generated electrons on the catalyst surface *via* the two-electron transfer pathway, while, the PPC-75 catalyst itself also serves as a sacrificial agent for consuming the photo-generated holes, leading to a high H_2O_2 production.

2. Experimental section

2.1 Materials

Proanthocyanidin (AR, 98%) was purchased from Shanghai Yuanye Biotechnology Co, Ltd. Ethanol (AR, 98%) and sulfuric acid (AR, 98%) were purchased from Shanghai Aladdin Biochemical Technology Co, Ltd. All reagents were used without further purification.

2.2 Synthetic strategy

Using an ethanol/water mixture as solvent, the catalyst (PPC-*X*, *X* = 75, 100, 125, 175) was synthesized by a hydrothermal method. The specific synthesis process is as follows: first, 0.2 g of proanthocyanidin (OPC) was added to 4.5 mL ultrapure water, followed by 0.5 mL ethanol and 1 mL sulfuric acid solution (3 mol L^{-1}), and sonicated for 20 min. The resulting mixed solution was transferred to a hydrothermal reaction vessel and sealed. Finally, the sealed reaction vessel was hydrothermally reacted at different temperatures for 10 h, and the reaction temperature was set to 75 °C, 100 °C, 125 °C, and 175 °C, respectively. After the reaction was complete, it was allowed to naturally cool to room temperature. The precipitate in the reactor was washed with ultra-pure water and centrifuged, and this was repeated three times. The washed precipitate was then dried at 60 °C for 36 h. Finally, the obtained polymer was ground to obtain a powdery single-dye polymer, labeled PPC-*X*, where *X* represents the polymerization temperature.

3. Results and discussion

3.1 Morphology and structure

The morphology of the catalyst was observed by a scanning electron microscope (SEM). It can be seen from Fig. 1(a)–(d)

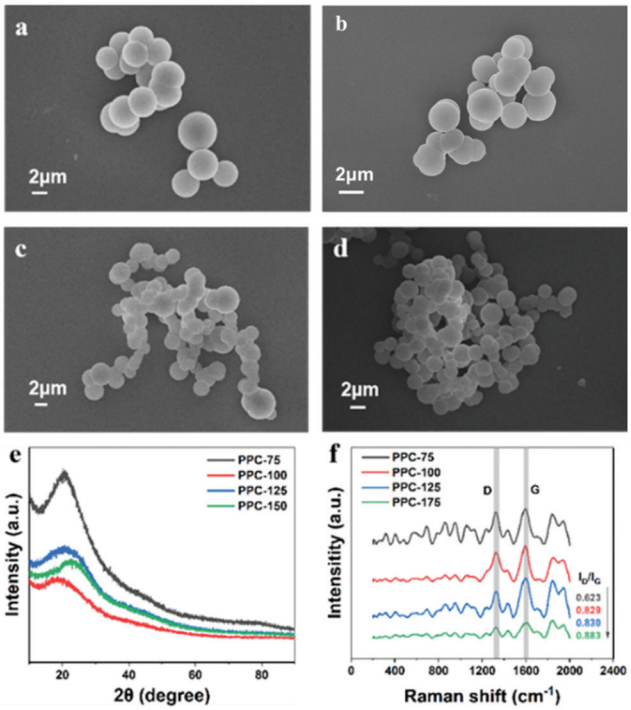

Fig. 1 SEM images of (a) PPC-75, (b) PPC-100, (c) PPC-125 and (d) PPC-175 catalysts. (e) XRD patterns, and (f) Raman spectra of PPC-*X* catalysts (*X* = 75, 100, 125, 175).

that the polymer PPC-*X* obtained at different polymerization temperatures is composed of microspheres. However, by comparison, it can be found that the catalyst polymerized at a lower temperature (PPC-75) has better dispersion than that polymerized at higher temperatures. The catalyst polymerized at a high temperature (PPC-175) has a wide range of agglomeration phenomena. Fig. 1(e) shows the X-ray diffraction (XRD) patterns of the single dye polymer catalysts PPC-*X*, where the diffraction peaks at 21° and 45° demonstrate that PPC-*X* was amorphous.[39,40]

Fig. 1(f) shows the Raman spectra of catalysts PPC-*X*, which displays two peaks centered at 1360 cm^{-1} and 1600 cm^{-1}, corresponding to the D band with sp^3 defect and the G band caused by the in-plane vibration of sp^2 carbon. The ratio of the D band to G band (I_D/I_G) indicates the defect characteristics of the catalyst. As shown in Fig. 1(f), the I_D/I_G ratio increases with the increase in temperature, which indicates that defects are more likely to occur at high temperatures. Therefore, when the temperature is too high, there are likely to be numerous defects, which is not conducive to the catalytic performance of the sample. The Fourier transform infrared spectroscopy in Fig. S1(a) (ESI†) indicates that the single dye polymer catalyst (PPC-*X*) obtained at different polymerization temperatures has similar infrared spectra, and the surface of the materials contains functional groups such as C–O, C═C, C═O, and C–OH bonds. Fig. S1(b), ESI† shows the FT-IR spectra of OPC and PPC-100. It can be seen from the FT-IR spectrum of OPC that it contains functional groups such as C–O, –Ph, and C–OH bonds. Compared with the FT-IR spectrum of OPC, the FT-IR

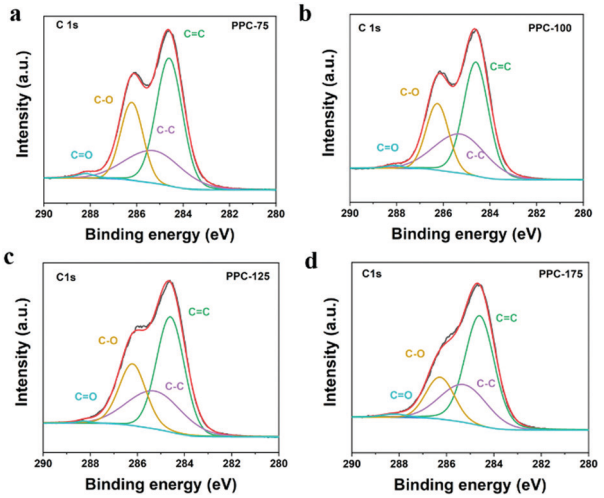

Fig. 2 C 1s spectra of PPC-*X* catalysts. (a), (b), (c) and (d) for PPC-75, PPC-100, PPC-125 and PPC-175, respectively.

spectrum of PPC-100 has a slight difference, with the peak at 1650 cm^{-1} corresponding to the C═O bond of the catalyst. The morphology of the single-dye polymer catalyst was further analyzed by transmission electron microscopy, and the results are shown in Fig. S2(a), ESI.† It can be seen that the surface of the microspheres composed of the polymer PPC-100 is relatively smooth, accompanied by some lamellar structures peeled off from the microspheres in the catalyst. Fig. S2(b) (ESI†) shows the particle size distribution of the single-dye polymer PPC-100, indicating that the average particle size of the polymer is mainly about 2500 nm.

The functional groups and bond energies of the catalysts were further analyzed by X-ray photoelectron spectroscopy (XPS). Fig. 2 shows the C 1s spectra of different catalysts. It can be seen from Fig. 2 that the C 1s spectra of the catalysts obtained at different temperatures can be fitted to four peaks located at 284.6, 285.3, 286.3, and 288.2 eV, corresponding to the C═C, C–C, C–O and C═O of the polymer components.[41,42] From the C 1s spectra of OPC in Fig. S8 (ESI†), it can be seen that the C 1s spectra of the catalysts obtained at different temperatures can be fitted into three peaks located at 284.6, 285.3, and 286.3 eV, corresponding to the C═C, C–C, and C–O components of the polymer. This result is consistent with the FT-IR spectra. The elemental analysis in Table S1 (ESI†) shows that all catalysts were composed of C, H, O, and S, and the S comes from the residual sulfuric acid on the surface of the catalyst. Simultaneously, it can be seen that the content of C in the polymer increases first and then decreases with the increase in the polymerization temperature, and reaches a maximum value when the polymerization temperature is 100 °C. The thermogravimetric spectrum of PPC-100 is shown in Fig. S7 (ESI†). When the temperature reaches 900 °C, the decomposition of PPC-100 is complete, and the carbon content was found to be 27.60%.

3.2 Band structure

To determine the band location of the catalyst, the ionization potential of catalyst PPC-100 was determined by ultraviolet photoelectron spectroscopy (UPS) to further explore the band structure of the sample. As shown in Fig. 3(a), the valence band (VB) position of the catalyst PPC-100 can be obtained at 5.76 eV by subtracting the spectral width of the ultraviolet photoelectron spectrum of He I from the excitation energy (21.22 eV); the conduction band (CB) position can be further calculated at 4.07 eV through the bandgap.[43] To better display the relationship between the conduction band/valence band of the catalyst and the redox potential of H_2O and O_2, the unit is converted from eV into electrochemical potential energy V according to the reference standard, where 0 V (*vs.* RHE) equals −4.44 eV (*vs.* Evac). As shown in Fig. 3(b), the CB of single-dye polymer PPC-100 is higher than the level of H_2O_2 produced by oxygen reduction, and the VB is lower than the level of O_2 produced by water oxidation, but it cannot reach the level of H_2O_2 produced by water oxidation. Therefore, it can be inferred that the catalyst can theoretically achieve the reduction reaction of O_2 and the oxidation reaction of water. Fig. 3(c) shows the UV-Vis absorption spectra of the catalysts PPC-*X*. It can be seen from the figure that the as-prepared single-dye polymer photocatalyst PPC-*X* has strong absorption in the ultraviolet and near-infrared regions, and its absorption value reaches a maximum value at about 600 nm, indicating that the catalyst can effectively utilize solar energy. In addition, it can also be seen from Fig. 3(c) that with the increase in the polymerization temperature, the optimal absorption wavelength of the catalyst first increases and then decreases, and the optimal absorption wavelength can reach 640 nm for PPC-100. The Tauc diagram obtained by the UV-Vis absorption spectrum can be used to calculate the optical band gap of a catalyst.[24,44] The $(\alpha h\nu)^2$–$h\nu$ curve obtained by the UV-Vis absorption spectrum is shown in Fig. 3(d). The curve shows a good linear relationship, indicating that photocatalyst PPC-*X* is a direct bandgap material. The bandgap of photocatalyst PPC-100 is 1.69 eV. The bandgap of photocatalyst PPC-175 is 1.93 eV. A low bandgap is more favorable for the generation of photogenic charge, which

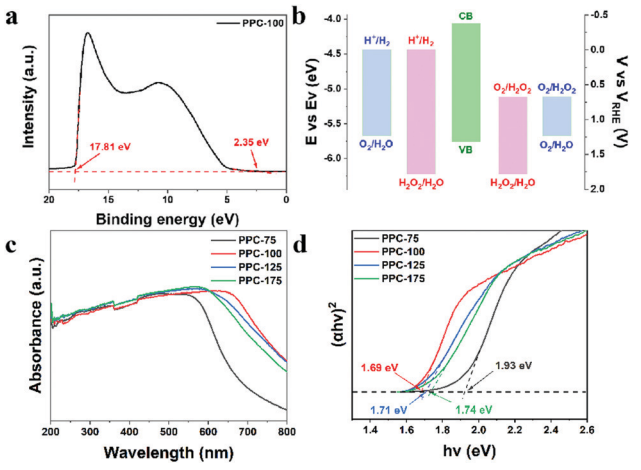

Fig. 3 (a) UPS spectrum of catalyst PPC-100. (b) Energy band structure of catalyst PPC-100 and the redox energy levels of water and O_2. (c) UV-Vis spectra and (d) the $(\alpha h\nu)^2$–$h\nu$ curves of polymer catalysts PPC-*X* (*X* = 75, 100, 125, 175).

improves the photocatalytic activity of the catalyst and completes the conversion of solar energy.

Due to the existence of defects in carbon materials, they have different band gaps. The oxidation and reduction state of catalysts can be studied by cyclic voltammetry (CV), and the band structure of the catalyst can be further deduced. Fig. 4 shows the CV curve of catalysts PPC-*X*. It can be seen from Fig. 4(a) that PPC-75 has multiple oxidation peaks, which are 1.66 and 1.91 V. However, other catalysts PPC-100, PPC-125, and PPC-175 have only one, at 1, 68, 1.7 and 1.69 V, respectively. The multiple oxidation levels occurring in the catalyst PPC-75 are due to the unfixed type of defects.

3.3 Photochemical properties

As shown in Fig. S3 (ESI†), all PPC-X samples generated photocurrent once exposed to light, indicating that all the polymer catalysts generate photocarriers under light conditions. In addition, by comparing the samples obtained at different temperatures, it was found that catalyst PPC-100 produced the maximum photocurrent under light conditions, while catalyst PPC-175 produced the minimum photocurrent under the light conditions, indicating that catalyst PPC-100 has the best photoresponse performance, which provides a basis for its photocatalytic application.

3.4 The transient photovoltage (TPV) measurements

As shown in Fig. 5(a), PPC-100 has the strongest photovoltage, indicating that after excitation, PPC-100 generates more photocharge compared to other catalysts, which is conducive to oxygen reduction in the H_2O_2 generation process. As shown in Fig. 5(b), t_{max} represents the time required from lighting up to maximum charge extraction. There is no significant difference between each catalyst, indicating that there is little difference in the photo-charge transfer rate. Fig. 5(c) shows the maximum charge extraction amount *A*, which represents the maximum value of photogenerated charge excited on the surface of the catalyst. In Fig. 5(f), the A value of PPC-100 is significantly higher than that of PPC-75 (A_1 = 0.098), PPC-125 (A_3 = 0.108), and PPC-175 (A_4 = 0.087), indicating that PPC-100 had better photo-charge extraction ability. Fig. 5(d) shows the τ values of different catalysts. Here, τ represents the time decay constant of the photo-charge. The larger the τ value is, the longer the lifetime of the photo-charge is.[45] It can be seen from Fig. 5(d) that PPC-100, PPC-125, and PPC-175 have only one attenuation stage, while PPC-75 has two attenuation stages, which are composed of a fast decay process (τ_1 = 0.066 ms) and a slow decay process (τ_2 = 0.168 ms), which may be related to

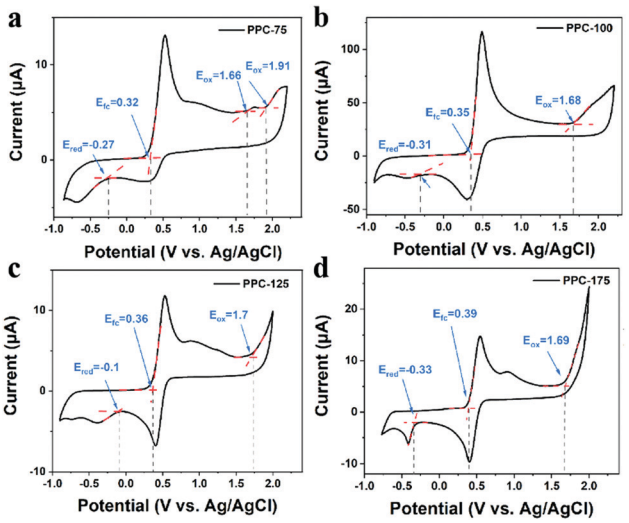

Fig. 4 (a) The CV curve of polymer catalyst PPC-75 (the oxidation states of the PPC-75 catalyst are 1.66 and 1.91 V, and the reduction state of the PPC-75 catalyst is −0.27 V). (b) The CV curve of polymer catalyst PPC-100 (the oxidation state of the PPC-100 catalyst is 1.68 V, and the reduction state of the PPC-100 catalyst is −0.31 V). (c) The CV curve of polymer catalyst PPC-125 (the oxidation state of the PPC-125 catalyst is 1.7 V, and the reduction state of the PPC-125 catalyst is −0.1 V). (d) The CV curve of polymer catalyst PPC-175 (the oxidation state of the PPC-175 catalyst is 1.69 V, and the reduction state of the PPC-175 catalyst is −0.33 V).

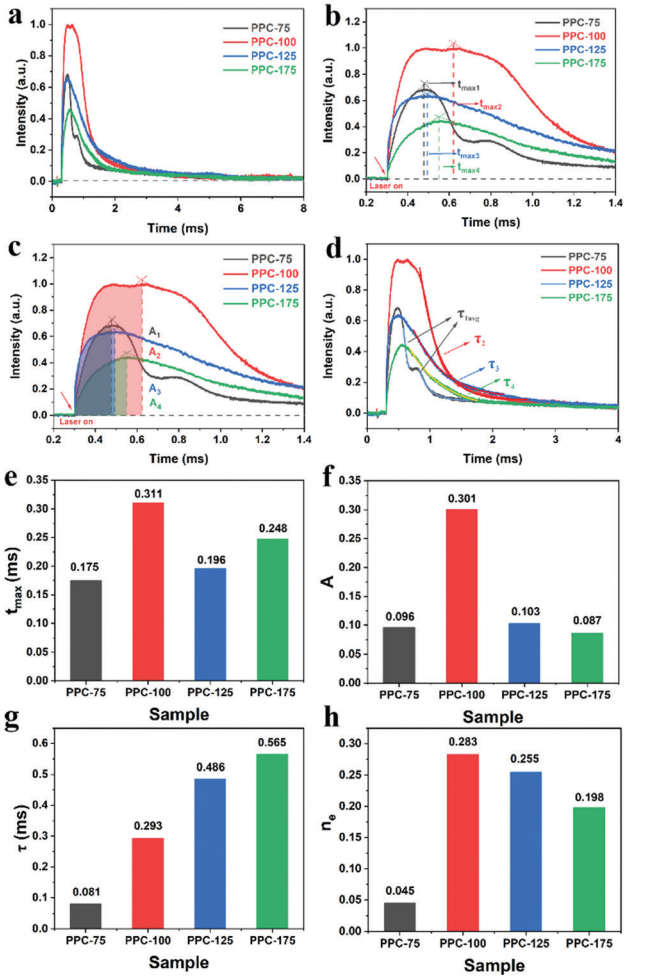

Fig. 5 (a) Comparison of the TPV with PPC-75, PPC-100, PPC-125 and PPC-175. (b) Maximum charge extraction time (t_{max}) of PPC-75, PPC-100, PPC-125 and PPC-175. (c) Charge extraction of PPC-75, PPC-100, PPC-125 and PPC-175. (d) The charge recombination of PPC-75, PPC-100, PPC- 125 and PPC-175. (e) Maximum charge extraction time (t_{max}). (f) The maximum charge extraction (A). (g) Charge attenuation time (τ). (h) Surface effective charge (n_e).

the heterogeneity of components. The average decay constant of PPC-75 (τ_{2avg} = 0.081 ms) is calculated by a formula in ESI.†

The signal characteristics of TPV indicate that it is a typical non-static signal. Fig. 6(a) shows the FFT curve of PPC-100. It can be seen that the curve reaches its maximum amplitude when the frequency is close to zero, which is a typical non-static signal characteristic. To further analyze the frequency and time characteristics of this non-static signal, we adopted the continuous wavelet transform (CWT) based on Bior3.9 to analyze both time and frequency scales.[46] We selected three frequencies f = 2 Hz, f = 4 Hz, and f = 10 Hz, and the CWT signal in the whole-time scale is shown in Fig. 6(c). When f = 2 Hz, it has signal distribution in the time range from 0 to 5 ms, indicating that both the fast and slow process of charge transfer plays an important role in the overall process. When f = 4 Hz, the CWT signal range is 0–1.4 ms, indicating that the fast electron transfer process occupies the main part of charge transfer. When f = 10 Hz, the CWT signal only exists in the range of 0–0.4 ms, which proves that the fast electron transfer process only exists in the initial stage of the charge transfer process. Fig. 8(d) shows CWT signals at t = 0.21 ms, t = 0.75 ms, and t = 4.0 ms in different frequency ranges. When t = 0.21 ms, signals exist in the range of 0–12 Hz, indicating that charge transfer is composed of both fast and slow processes. However, when t = 0.75 ms, the signal range is reduced to 0–8 Hz, and the signal at this time is mainly a medium and low-frequency signal. As time continues to increase to t = 4 ms, only the low-frequency part (0–2 Hz) of the signal in Fig. 8(d) is left, and almost the whole charge transmission process is composed of the slow process.

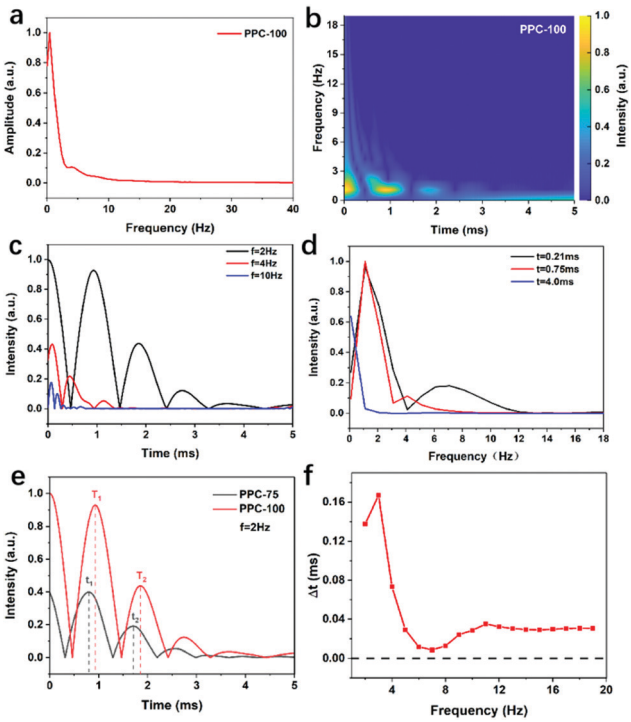

Fig. 6 (a) FT spectrum, (b) 2D CWT spectrum, (c) Intensity–frequency curves (t = 0.21, 0.75 and 4.0 ms) and (d) Intensity–time curves (f = 2, 4, and 10 Hz) of PPC-100, (e) Intensity–time curves of PPC-100, (f) Peak delay time (Δt) at different frequencies (f = 2, 3, 4, 5, 6, 7, 8, 9, 10, 11, 12, 13, 14, 15, 16, 17 and 18 Hz); here, the peak time of sample PPC-100 was used as the reference value.

We used the peak delay time (ΔT) of the intensity time curve to study the charge transfer process between the catalyst interfaces and determined the speed of the charge transfer process. Fig. 6(e) shows the comparison between the peak position of PPC-75 and PPC-100 at f = 2 Hz, and we observed the time scale delay of the peak position of PPC-100.[47] Fig. 6(f) shows the relationship between its peak delay time (ΔT) and frequency (see ESI† for the specific calculation method). It can be seen that the peak delay time (ΔT) is greater than zero in all frequency ranges, and the peak delay time (ΔT) of PPC-100, PPC125 and PPC-175 is also greater than zero in all frequency ranges (Fig. S4–S6, ESI†). These results indicate that the charge transfer process of PPC-100 is slower than that of the catalysts at other temperatures, and the slower charge transfer is helpful to the improvement of photogenic electron stability and catalytic activity.

3.5 Photocatalytic experiments

In the photocatalytic experiments, a multi-channel photocatalytic reaction system was used to evaluate the photocatalytic activity of the catalyst in a 40 mL glass bottle reactor with a visible light source, and the wavelength of visible light was $\lambda \geq 420$ nm, without adding any sacrificial agent or cocatalyst. In a typical catalytic reaction process, 10 mg catalyst was dispersed in 20 mL ultrapure water for 10 min by ultrasound, and then the reactor was placed in a multi-channel photocatalytic reaction system and exposed to visible light for 6 h at room temperature. After the reaction, the reaction solution was centrifuged and filtered, and then the H_2O_2 in the filtrate was quantitatively analyzed.

For the stability of the catalyst catalyzed reaction, the reactor was shaded and settled for 12 h after each illumination. After that, 10 mL supernatant was filtered to measure its hydrogen peroxide yield. The remaining solution and catalyst were dried thoroughly and then the cycling experiment was carried out. The cycle was repeated 5 times, each time under the same conditions, and the quantitative determination of hydrogen peroxide was carried out after each experiment.

According to the influence of the wavelength of light on the yield of H_2O_2 catalyzed by the catalyst, light source with different wavelengths was used to illuminate the catalyst, and the wavelengths were 365, 420, 485, 595, and 620 nm respectively. The reaction system comprised 10 mg PPC-100 dispersed in 20 mg ultrapure water, and the reaction time was 6 h. After the reaction, the yield of H_2O_2 in the system was quantitatively determined. To study the effects of different atmospheres on the yield of H_2O_2, gas bubbles were used to create different atmospheres. The reaction system with 10 mg catalyst was bubbled with N_2 and O_2 for 20 min to create an N_2 and O_2 saturated atmosphere. Then, the reaction system was sealed and placed in a multi-channel photocatalytic reaction system for 6 h. H_2O_2 in the system was quantitatively determined after

the reaction. To analyze the effect of adding a sacrificial agent on H_2O_2 production. Electron sacrificial agent, hole sacrificial agent, superoxide free radical capture agent, and hydroxyl free radical capture agent were added to the reaction system, respectively. During the reaction, 0.2 mmol of silver nitrate ($AgNO_3$), methanol (CH_3OH), benzoquinone (BQ), and *tert*-butanol (TBA) were added to the reaction system. H_2O_2 in the system was quantitatively determined after 6 h illumination. To validate the effect of the reaction environment on the catalytic activity of the catalyst, N_2, and O_2 bubbles were used to create different reaction environments. Taking N_2 as an example, the reaction system with dispersed catalyst PPC-100 was bubbled with N_2 for 30 min, so that the solution reached N_2 saturation. The reactor was then sealed and placed under visible light for 6 h. After the reaction, the H_2O_2 in the filtrate was quantitatively analyzed. For all the above methods, the quantitative determination of H_2O_2 was carried out using $KMnO_4$ titration. During the titration process, 10 mL of the filtered solution after completion of the reaction, was collected and titrated with 0.02 mol L^{-1} of $KMnO_4$ standard solution ($KMnO_4 : H_2SO_4 = 1:1$) until the solution turned red and did not fade for 30 s. Finally, the amount of H_2O_2 produced in the catalytic system was calculated according to the volume of potassium permanganate used in the titration.

3.6 Evaluation of catalytic activity

First, the photocatalytic activity of PPC-*X* was studied under different polymerization temperatures. As shown in Fig. 7(a), the catalyst PPC-100 obtained at the polymerization temperature of 100 °C had the highest catalytic activity, and its yield reached 1214 μmol g^{-1} h^{-1}. With the increase in the polymerization temperature, the catalytic activity of the obtained catalyst decreased. Among the as-prepared catalysts, catalyst PPC-175 had the lowest activity. It is worth noting that the H_2O_2 yield of PPC-75 is not significantly different from that of PPC-100, which is inconsistent with its less effective charge (n_e). Combined with the CV curve, we propose that the partially unoxidized part may act as a sacrificial agent, leading to higher H_2O_2 production. In addition, the conversion efficiency of solar energy to chemical energy (SCC) was calculated, and the SCC of the PPC-100 catalyst reached 0.15% (see ESI† for calculation details). Fig. 7(b) shows the cycling stability of the catalyst. It can be seen from Fig. 7(b) that the activity of the catalyst remains unchanged within the fifth cycle. In the fifth cycle, the H_2O_2 synthesis rate of catalyst PPC-100 was maintained at 1021 μmol g^{-1} h^{-1}. The results indicate that the single dye polymer PPC-100 has good photocatalytic stability. The FT-IR spectra of fresh PPC-100 and recovered PPC-100 are shown in Fig. S1(c) (ESI†). It can be seen that compared with the fresh PPC-100, the structure/functional groups of recovered PPC-100 have not changed. Fig. 7(c) shows the relationship between the amount of H_2O_2 synthesis and the time of catalyst PPC-100 in the photocatalytic reaction. As shown in Fig. 7(c), no H_2O_2 was detected under dark conditions, indicating the result of the photocatalytic reaction of catalyst when H_2O_2 is generated. Under light conditions, the yield of H_2O_2 increases linearly with the increase in time, indicating the dependence of the catalytic reaction on light, and also indicating the stability and persistence of the catalytic reaction. Fig. 9(d) shows the calculated apparent quantum yield of single-dye polymer PPC-100 at different wavelengths. It can be seen from the figure that the AQY value of catalyst PPC-100 at the wavelength 595 nm is the largest, reaching up to 0.43% (see ESI† for calculation details). In addition, by comparing the UV-visible absorption spectra of AQY with the catalyst at different wavelengths, it can be seen that the variation trend of AQY is consistent with the UV absorption, indicating that the catalyst carries out the photocatalytic reaction through bandgap excitation.

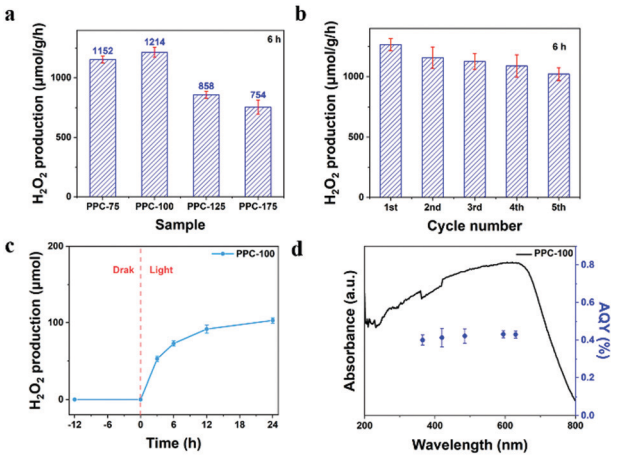

Fig. 7 (a) H_2O_2 production rates of different PPC-*X* catalysts. (b) Cyclic stability of catalyst PPC-100. (c) Relation of H_2O_2 yield of catalyst PPC-100 with time. (d) AQY of catalyst PPC-100 and its UV-Vis spectrum.

Fig. 8(a) reveals the yield of H_2O_2 under different sacrificial additives. Among them, $AgNO_3$, CH_3OH, benzoquinone (BQ), and *tert*-butanol (TBA) were used as the trapping agents of electrons (e^-), hole (h^+), superoxide radical ($^\bullet O_2^-$), and hydroxyl radical ($^\bullet OH$), respectively.[48,49] As shown in the figure, the yield of H_2O_2 decreased significantly with the addition of $AgNO_3$. The yield of H_2O_2 increased with the addition of CH_3OH. It can be said that H_2O_2 is formed by the reaction in which electrons are involved. When electrons are consumed, the activity decreases, while when holes are captured, the separation efficiency of photogenerated charge is improved, resulting in a higher H_2O_2 yield. In addition, when benzoquinone was added, the content of H_2O_2 in the reaction solution was very low, and the addition of *tert*-butanol had almost no effect on the catalytic activity of PPC-100. These results indicate that when catalyst PPC-100 performs photocatalytic reaction, photogenerated electrons reduce O_2, producing H_2O_2 ($O_2 \rightarrow {}^\bullet O_2^- \rightarrow H_2O_2$) and photogenerated holes participate in the water oxidation reaction, releasing O_2 ($H_2O \rightarrow O_2$).

The catalytic activity of single dye catalyst PPC-100 in different atmospheres was studied. As shown in Fig. 8(b), the yield of H_2O_2 increased in the O_2 environment, while that in nitrogen was greatly reduced. This is because, in the O_2 saturated environment, sufficient O_2 ensures the oxygen reduction reaction, improving the electron utilization efficiency, and then increasing the yield of

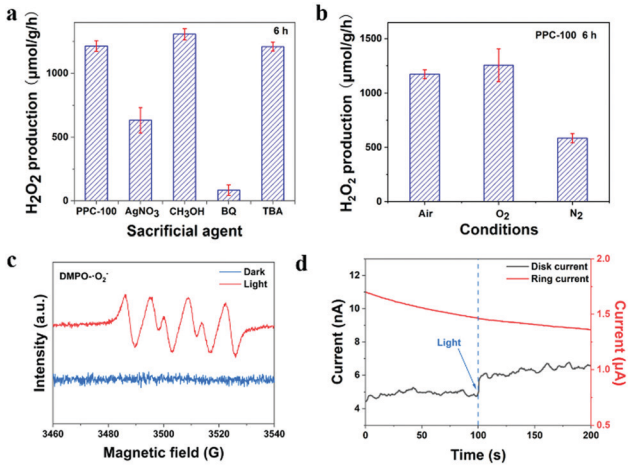

Fig. 8 (a) H_2O_2 yield of catalyst PPC-100 which was added with different sacrificial agents. (b) The catalytic activity of catalysts under different atmospheres. (c) EPR spectra of catalyst PPC-100 to $^{\bullet}O_2^-$ under dark and light conditions. (d) The current–time curves of catalyst PPC-100.

H_2O_2. In the N_2 saturated environment, O_2 is mainly generated by the oxidation reaction of water, and this O_2 then participates in the oxygen reduction reaction to produce H_2O_2. Due to the limitation of the water oxidation rate and oxygen content, the catalytic activity of the catalyst is limited, and the yield of H_2O_2 decreases. Therefore, it can be preliminarily inferred that the photocatalytic reaction is the oxygen reduction reaction involving O_2.

The free radicals in the reaction were further confirmed by electron paramagnetic resonance. As shown in Fig. 8(c), under dark conditions, no superoxide radical was detected, while under light conditions, four distinct superoxide radical signals were observed. The results show that the photocatalytic reaction of PPC-100 is the reaction of H_2O_2 production oxygen reduction. The process of H_2O_2 production was further confirmed by the rotating ring electrode. As shown in Fig. 8(d), in pure water saturated with N_2, the disk current of the rotating ring disk electrode increased significantly after the addition of light, while the ring current did not change after the addition of light. Alternatively, during the oxidation of water, no H_2O_2 is produced. The number of electrons transferred in the process of water oxidation is 4.[50] The results show that the oxidation of water only releases O_2 but does not produce H_2O_2.

Based on the above results and analysis, a catalytic mechanism for single dye polymer catalysts PPC-75 and PPC-100 was proposed. As shown in Fig. 9(a), the catalyst generates a photogenerated charge under light excitation. The conduction band electrons react with O_2 in the water, reducing O_2 to H_2O_2. The holes in the valence band participate in the oxidation reaction of water, releasing O_2. The reaction mechanism of PPC-75 is shown in Fig. 9(b). Oxygen reduction produces hydrogen peroxide in the same way as PPC-100, but the reaction of water oxidation depletion holes is partially replaced by catalyst self-sacrifice, which corresponds to a two-stage attenuation in the TPV test, as shown in Fig. 7(a). Moreover, due to the presence of the self-sacrificial reaction, the hydrogen peroxide production of PPC-75 increases significantly, second only to that of PPC-100.

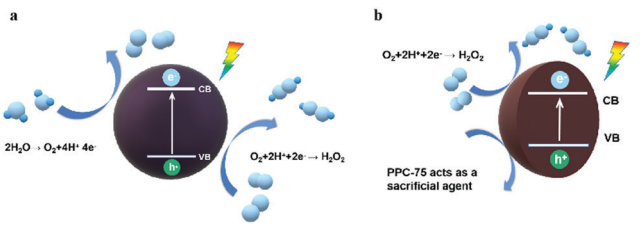

Fig. 9 (a) The mechanism diagram of photocatalytic H_2O_2 production over the PPC-100 photocatalyst. (b) Possible mechanism diagram of photocatalytic H_2O_2 production over the PPC-75 photocatalyst.

4. Conclusions

In this study, single-dye polymer catalyst PPC-*X* was designed and synthesized by a hydrothermal polymerization method, in which, the catalyst PPC-100 shows the best catalytic activity for H_2O_2 photoproduction. The conversion efficiency of solar energy to hydrogen energy of the PPC-100 catalyst reached 0.15% at the light intensity of 32.6 mW cm^{-2}, and the production rate of H_2O_2 reached 1214 μmol g^{-1} h^{-1}. Combined with various characterization and transient photovoltage tests, the diverse catalytic behavior of the dye-based polymer metal-free catalysts as well as the photocatalytic reaction mechanism was demonstrated. Under light excitation, for PPC-100, PPC-125, and PPC-175, the catalyst reduced O_2 to produce H_2O_2 through the two-electron transfer pathway and oxidized water to release O_2 through the four-electron transfer pathway. For the PPC-75 catalyst, the O_2 was reduced by photo-generated electrons on the catalyst surface *via* the two-electron transfer pathway, while the PPC-75 catalyst itself also served as a sacrificial agent. This work provides a practical research example and idea for an in-depth understanding and design of efficient polymer-based photocatalysts.

Author contributions

The manuscript was written through contributions of all authors. All authors have given approval to the final version of the manuscript.

Conflicts of interest

The authors declare no conflict of interest.

Acknowledgements

This work is supported by National Key R&D Program of China (2020YFA0406104, 2020YFA0406101), National MCF Energy R&D Program of China (2018YFE0306105), Innovative Research Group Project of the National Natural Science Foundation of China (51821002), National Natural Science Foundation of China (51725204, 21771132, 51972216, 52041202), Natural

Science Foundation of Jiangsu Province (BK20190041), Key-Area Research and Development Program of Guangdong Province (2019B010933001), Collaborative Innovation Center of Suzhou Nano Science & Technology, the 111 Project, and Suzhou Key Laboratory of Functional Nano & Soft Materials.

References

1 X. Chen, Y. Kondo, Y. Kuwahara, K. Mori, C. Louis and H. Yamashita, Metal–organic framework-based nanomaterials for photocatalytic hydrogen peroxide production, *Phys. Chem. Chem. Phys.*, 2020, **22**, 14404–14414.

2 H. Song, L. Wei, C. Chen, C. Wen and F. Han, Photocatalytic production of H_2O_2 and its in situ utilization over atomic-scale Au modified MoS_2 nanosheets, *J. Catal.*, 2019, **376**, 198–208.

3 Y. Peng, L. Wang, Y. Liu, H. Chen, J. Lei and J. Zhang, Visible-light-driven photocatalytic H_2O_2 production on g-C_3N_4 loaded with CoP as a noble metal free cocatalyst, *Eur. J. Inorg. Chem.*, 2017, 4797–4802.

4 Z. Li, N. Xiong and G. Gu, Fabrication of a full-spectrum-response $Cu_2(OH)_2CO_3$/g-C_3N_4 heterojunction catalyst with outstanding photocatalytic H_2O_2 production performance *via* a self-sacrificial method, *Dalton Trans.*, 2018, **48**, 182–189.

5 S. Li, G. Dong, R. Hailili, L. Yang, Y. Li, F. Wang, Y. Zeng and C. Wang, Effective photocatalytic H_2O_2 production under visible light irradiation at g-C_3N_4 modulated by carbon vacancies, *Appl. Catal., B*, 2016, **190**, 26–35.

6 Y. Wang, S. Hu, Q. Li, G. Gu, Y. Zhao, H. Liang and W. Li, One step synthesis of high-efficiency AgBr–Br-g-C_3N_4 composite catalysts for photocatalytic H_2O_2 production *via* two channel pathway, *RSC Adv.*, 2018, **8**, 36903–36909.

7 G. Wu, S. Hu, Z. Han, C. Liu and Q. Li, The effect of Ni(I)–N active sites on the photocatalytic H_2O_2 production ability over nickel doped graphitic carbon nitride nanofibers, *New J. Chem.*, 2017, **41**, 15289–15297.

8 Y. Fu, C. a. Liu, M. Zhang, C. Zhu, H. Li, H. Wang, Y. Song, H. Huang, Y. Liu and Z. Kang, Photocatalytic H_2O_2 and H_2 generation from living chlorella vulgaris and carbon micro particle comodified g-C_3N_4, *Adv. Energy Mater.*, 2018, **8**, 1802525.

9 C. Zhu, M. Zhu, Y. Sun, Y. Zhou, J. Gao, H. Huang, Y. Liu and Z. Kang, Carbon-supported oxygen vacancy-rich Co_3O_4 for robust photocatalytic H_2O_2 Production *via* coupled water oxidation and oxygen reduction reaction, *ACS Appl. Energy Mater.*, 2019, **2**, 8737–8746.

10 Y. Liu, Y. Zhao, Y. Sun, J. Cao, H. Wang, X. Wang, H. Huang, M. Shao, Y. Liu and Z. Kang, A 4e-2e- cascaded pathway for highly efficient production of H_2 and H_2O_2 from water photo-splitting at normal pressure, *Appl. Catal., B*, 2020, **270**, 118875.

11 L. Zheng, J. Zhang, Y. H. Hu and M. Long, Enhanced photocatalytic production of H_2O_2 by Nafion coatings on S,N-codoped graphene-quantum-dots-modified TiO_2, *J. Phys. Chem. C*, 2019, **123**, 13693–13701.

12 L. Yang, G. Dong, D. L. Jacobs, Y. Wang, L. Zang and C. Wang, Two-channel photocatalytic production of H_2O_2 over g-C_3N_4 nanosheets modified with perylene imides, *J. Catal.*, 2017, **352**, 274–281.

13 L. Zheng, H. Su, J. Zhang, L. S. Walekar, H. Vafaei Molamahmood, B. Zhou, M. Long and Y. H. Hu, Highly selective photocatalytic production of H_2O_2 on sulfur and nitrogen co-doped graphene quantum dots tuned TiO_2, *Appl. Catal., B*, 2018, **239**, 475–484.

14 J. Cao, H. Wang, Y. Zhao, Y. Liu, Q. Wu, H. Huang, M. Shao, Y. Liu and Z. Kang, Phosphorus-doped porous carbon nitride for efficient sole production of hydrogen peroxide *via* photocatalytic water splitting with a two-channel pathway, *J. Mater. Chem. A*, 2020, **8**, 3701–3707.

15 Y. Fu, C. a. Liu, C. Zhu, H. Wang, Y. Dou, W. Shi, M. Shao, H. Huang, Y. Liu and Z. Kang, High-performance NiO/g-C_3N_4 composites for visible-light-driven photocatalytic overall water splitting, *Inorg. Chem. Front.*, 2018, **5**, 1646–1652.

16 Y. Yang, Z. Zeng, G. Zeng, D. Huang, R. Xiao, C. Zhang, C. Zhou, W. Xiong, W. Wang, M. Cheng, W. Xue, H. Guo, X. Tang and D. He, Ti_3C_2 Mxene/porous g-C_3N_4 interfacial Schottky junction for boosting spatial charge separation in photocatalytic H_2O_2 production, *Appl. Catal., B*, 2019, **258**, 117956.

17 C. Zhu, C. a. Liu, Y. Fu, J. Gao, H. Huang, Y. Liu and Z. Kang, Construction of CDs/CdS photocatalysts for stable and efficient hydrogen production in water and seawater, *Appl. Catal., B*, 2019, **242**, 178–185.

18 Z.-Q. Li, Y. Wang, Z.-Q. Wu, M.-Y. Wu and X.-H. Xia, Bioinspired multivalent ion responsive nanopore with ultrahigh ion current rectification, *J. Phys. Chem. C*, 2019, **123**, 13687–13692.

19 M. Teranishi, R. Hoshino, S. Naya and H. Tada, Gold-nanoparticle-loaded carbonate-modified titanium(IV) oxide surface: Visible-light-driven formation of hydrogen peroxide from oxygen, *Angew. Chem., Int. Ed.*, 2016, **55**, 12773–12777.

20 H. Hou, X. Zeng and X. Zhang, Production of hydrogen peroxide by photocatalytic processes, *Angew. Chem., Int. Ed.*, 2020, **59**, 17356–17376.

21 Z. Mo, X. Zhu, Z. Jiang, Y. Song, D. Liu, H. Li, X. Yang, Y. She, Y. Lei, S. Yuan, H. Li, L. Song, Q. Yan and H. Xu, Porous nitrogen-rich g-C_3N_4 nanotubes for efficient photocatalytic CO_2 reduction, *Appl. Catal., B*, 2019, **256**, 117854.

22 Z. Li, Y. Zhi, P. Shao, H. Xia, G. Li, X. Feng, X. Chen, Z. Shi and X. Liu, Covalent organic framework as an efficient, metal-free, heterogeneous photocatalyst for organic transformations under visible light, *Appl. Catal., B*, 2019, **245**, 334–342.

23 Z. Wei, M. Liu, Z. Zhang, W. Yao, H. Tan and Y. Zhu, Efficient visible-light-driven selective oxygen reduction to hydrogen peroxide by oxygen-enriched graphitic carbon nitride polymers, *Energy Environ. Sci.*, 2018, **11**, 2581–2589.

24 Z. He, C. Kim, L. Lin, T. H. Jeon, S. Lin, X. Wang and W. Choi, Formation of heterostructures *via* direct growth CN on h-BN porous nanosheets for metal-free photocatalysis, *Nano Energy*, 2017, **42**, 58–68.

25 K. Zhao, Y. Su, X. Quan, Y. Liu, S. Chen and H. Yu, Enhanced H_2O_2 production by selective electrochemical

reduction of O_2 on fluorine-doped hierarchically porous carbon, *J. Catal.*, 2018, **357**, 118–126.

26 J. Liu, Y. Liu, N. Y. Liu, Y. Z. Han, X. Zhang, H. Huang, Y. Lifshitz, S. T. Lee, J. Zhong and Z. H. Kang, Metal-free efficient photocatalyst for stable visible water splitting *via* a two-electron pathway, *Science*, 2015, **347**, 970–974.

27 S. Gogoi and N. Karak, Solar-driven hydrogen peroxide production using polymer-supported carbon dots as heterogeneous catalyst, *Nano-Micro Lett.*, 2017, **9**, 40.

28 C. Krishnaraj, H. S. Jena, L. Bourda, A. Laemont, P. Pachfule, J. Roeser, C. V. Chandran, S. Borgmans, S. M. J. Rogge, K. Leus, C. V. Stevens, J. A. Martens, V. Van Speybroeck, E. Breynaert, A. Thomas and P. Van der Voort, Strongly reducing (diarylamino)benzene-based covalent organic framework for metal-free visible light photocatalytic H_2O_2 generation, *J. Am. Chem. Soc.*, 2020, **142**, 20107–20116.

29 W.-C. Hou and Y.-S. Wang, Photocatalytic generation of H_2O_2 by graphene oxide in organic electron donor-free condition under sunlight, *ACS Sustainable Chem. Eng.*, 2017, **5**, 2994–3001.

30 J. Xiong, X. Li, J. Huang, X. Gao, Z. Chen, J. Liu, H. Li, B. Kang, W. Yao and Y. Zhu, CN/rGO@BPQDs high-low junctions with stretching spatial charge separation ability for photocatalytic degradation and H_2O_2 production, *Appl. Catal., B*, 2020, **266**, 118602.

31 L. Zhou, J. Lei, F. Wang, L. Wang, M. R. Hoffmann, Y. Liu, S.-I. In and J. Zhang, Carbon nitride nanotubes with in situ grafted hydroxyl groups for highly efficient spontaneous H_2O_2 production, *Appl. Catal., B*, 2021, **288**, 119993.

32 S. Zhao, T. Guo, X. Li, T. Xu, B. Yang and X. Zhao, Carbon nanotubes covalent combined with graphitic carbon nitride for photocatalytic hydrogen peroxide production under visible light, *Appl. Catal., B*, 2018, **224**, 725–732.

33 Y. Zhao, Y. Liu, J. Cao, H. Wang, M. Shao, H. Huang, Y. Liu and Z. Kang, Efficient production of H_2O_2*via* two-channel pathway over ZIF-8/C_3N_4 composite photocatalyst without any sacrificial agent, *Appl. Catal., B*, 2020, **278**, 119829.

34 J. Zhang, C. Yu, J. Lang, Y. Zhou, B. Zhou, Y. H. Hu and M. Long, Modulation of Lewis acidic–basic sites for efficient photocatalytic H_2O_2 production over potassium intercalated tri-*s*-triazine materials, *Appl. Catal., B*, 2020, **277**, 119225.

35 Y. L. Wong, J. M. Tobin, Z. Xu and F. Vilela, Conjugated porous polymers for photocatalytic applications, *J. Mater. Chem. A*, 2016, **4**, 18677–18686.

36 X. Yu, B. Viengkeo, Q. He, X. Zhao, Q. Huang, P. Li, W. Huang and Y. Li, Electronic tuning of covalent triazine framework nanoshells for highly efficient photocatalytic H_2O_2 production, *Adv. Sustainable Syst.*, 2021, **5**, 2100184.

37 Y. Shiraishi, T. Takii, T. Hagi, S. Mori, Y. Kofuji, Y. Kitagawa, S. Tanaka, S. Ichikawa and T. Hirai, Resorcinol-formaldehyde resins as metal-free semiconductor photocatalysts for solar-to-hydrogen peroxide energy conversion, *Nat. Mater.*, 2019, **18**, 985–993.

38 L. Chen, L. Wang, Y. Wan, Y. Zhang, Z. Qi, X. Wu and H. Xu, Acetylene and diacetylene functionalized covalent triazine frameworks as metal-free photocatalysts for hydrogen peroxide production: A new two-electron water oxidation pathway, *Adv. Mater.*, 2020, **32**, e1904433.

39 N. Karikalan, M. Elavarasan and T. C. K. Yang, Effect of cavitation erosion in the sonochemical exfoliation of activated graphite for electrocatalysis of acebutolol, *Ultrason. Sonochem.*, 2019, **56**, 297–304.

40 B. Murugesan, N. Pandiyan, M. Arumugam, M. Veerasingam, J. Sonamuthu, A. R. Jeyaraman, S. Samayanan and S. Mahalingam, Two dimensional graphene oxides converted to three dimensional P, N, F and B, N, F tri-doped graphene by ionic liquid for efficient catalytic performance, *Carbon*, 2019, **151**, 53–67.

41 S. Asadzadeh-Khaneghah, A. Habibi-Yangjeh and M. Abedi, Decoration of carbon dots and AgCl over g-C_3N_4 nanosheets: Novel photocatalysts with substantially improved activity under visible light, *Sep. Purif. Technol.*, 2018, **199**, 64–77.

42 Y. Li, W. Ho, K. Lv, B. Zhu and S. C. Lee, Carbon vacancy-induced enhancement of the visible light-driven photocatalytic oxidation of NO over g-C_3N_4 nanosheets, *Appl. Surf. Sci.*, 2018, **430**, 380–389.

43 R. Yang, X. Teng, X. Lu, X. Li, L. Kuai, R. Zhang, C. Zhang and Z. Wu, Effect of interface contact between C and C_3N_4 on photocatalytic water splitting, *Catal. Lett.*, 2018, **148**, 1435–1444.

44 G.-h. Moon, M. Fujitsuka, S. Kim, T. Majima, X. Wang and W. Choi, Eco-friendly photochemical production of H_2O_2 through O_2 reduction over carbon nitride frameworks incorporated with multiple heteroelements, *ACS Catal.*, 2017, **7**, 2886–2895.

45 Y. Li, Y. Zhao, J. Wu, Y. Han, H. Huang, Y. Liu and Z. Kang, Photo-charge regulation of metal-free photocatalyst by carbon dots for efficient and stable hydrogen peroxide production, *J. Mater. Chem. A*, 2021, **9**, 25453–25462.

46 Y. Han, J. Wu, Y. Li, X. Gu, T. He, Y. Zhao, H. Huang, Y. Liu and Z. Kang, Carbon dots enhance the interface electron transfer and photoelectrochemical kinetics in TiO_2 photoanode, *Appl. Catal., B*, 2022, **304**, 120983.

47 H. Nie, Y. Liu, Y. Li, K. Wei, Z. Wu, H. Shi, H. Huang, Y. Liu, M. Shao and Z. Kang, In-situ transient photovoltage study on interface electron transfer regulation of carbon dots/$NiCo_2O_4$ photocatalyst for the enhanced overall water splitting activity, *Nano Res.*, 2022, **15**, 1786–1795, DOI: **10.1007/s12274-021-3723-2**.

48 S. Z. Hu, X. Y. Qu, P. Li, F. Wang, Q. Li, L. J. Song, Y. F. Zhao and X. X. Kang, Photocatalytic oxygen reduction to hydrogen peroxide over copper doped graphitic carbon nitride hollow microsphere: The effect of Cu(I)–N active sites, *Chem. Eng. J.*, 2018, **334**, 410–418.

49 Y. Y. Liu, Z. J. Liao, X. L. Ma and Z. H. Xiang, Ultrastable and efficient visible-light-driven hydrogen production based on donor–acceptor copolymerized covalent organic polymer, *ACS Appl. Mater. Interfaces*, 2018, **10**, 30698–30705.

50 L. Luo, Z.-j. Wang, X. Xiang, D. Yan and J. Ye, Selective activation of benzyl alcohol coupled with photoelectrochemical water oxidation *via* a radical relay strategy, *ACS Catal.*, 2020, **10**, 4906–4913.